Applied Physics Letters ARTICLE scitation.org/journal/apl

Gas breakdown and its scaling law in microgaps with multiple concentric cathode protrusions

Cite as: Appl. Phys. Lett. **114**, 014102 (2019); doi: 10.1063/1.5077015
Submitted: 23 October 2018 · Accepted: 26 December 2018 · Published Online: 09 January 2019

Yangyang Fu,[1,2,a)] Peng Zhang,[2] Janez Krek,[1] and John P. Verboncoeur[1,2]

AFFILIATIONS

[1] Department of Computational Mathematics, Science and Engineering, Michigan State University, East Lansing, Michigan 48824, USA
[2] Department of Electrical and Computer Engineering, Michigan State University, East Lansing, Michigan 48824, USA

[a)] E-mail: fuyangya@egr.msu.edu

ABSTRACT

This paper reports gas breakdown characteristics in microgaps with multiple concentric protrusions on the cathode in the transition from the Townsend to the subnormal glow discharge regime, using a two-dimensional hydrodynamic model. The effects of the protrusion aspect ratio, height, and protrusion spacing on the breakdown voltage are investigated. The results show that when the protrusion spacing is small, the shielding effect can play a more important role in the breakdown voltage rather than the protrusion aspect ratio; the breakdown voltage is more sensitive to the protrusion height and can be assessed by the shortest gap distance. Increasing the protrusion spacing decreases the shielding effect, which lowers the breakdown voltage in both low- and high-pressure regimes. It is found that the breakdown scaling law still holds in geometrically similar microgaps with multiple cathode protrusions despite the electric field distortion.

Gas breakdown in microscale gaps has become an active area of investigation with growing attention on microdischarges and their applications, including micro-electro-mechanical systems, plasma display panels, micro-switches, and microelectronic devices.[1–4] Even though gas breakdown has been extensively investigated in gaps between finished planar electrodes, electrode surface defects cannot be completely avoided and the discharge properties can be greatly affected by the surface defects. As the gap distance shrinks to microscales, the electrode surface status, such as the surface roughness and the surface protrusion, becomes more pronounced with respect to the breakdown processes.[5–7] Previously, the effect of the electrode defects was investigated mostly for streamer and spark breakdowns at high pressures,[8–10] assuming the electrode surface having a single protrusion or randomly generated textures,[11] and it was confirmed that the surface protrusion can cause a significant reduction in the voltage threshold.[12,13]

Recent advances in fabrication technologies, such as laser induced forward transfer (LIFT), enable manufacturing microdischarge devices with increasingly complicated high-resolution 3D structures.[14,15] Different morphologies of electrode surfaces have been produced by the deposition of dust plasma for studying the gas breakdown characteristics.[16] Apparently, a designed electrode surface morphology in discharge gaps can significantly change electric field distribution with local enhancements and thus adjust the transport of charged particles, which greatly impacts the breakdown characteristics. The microgap discharge is ignited and maintained by field emission when the electric field is on the order of 1 V/nm, whereas secondary electron emission is more important for weaker electric fields.[17–23] In recent years, theoretical, numerical, and experimental works were conducted on microscale breakdown, including characterizing the breakdown mode transition,[24,25] controlling the plasma to microstructure interaction,[26,27] and promoting the microdischarge uniformity.[28–30] It can be expected that with the emerging advances in fabrication technologies, microdischarge devices designed with more diverse and complicated structures will be a reality for various targets of controlling discharge behaviors. Understanding the breakdown characteristics with a given electrode morphology, as well as designing engineered electrode surface structures with desired breakdown characteristics, is important to achieve targeted system variability in microdischarge devices. In our previous studies,[31,32] microgap breakdowns were investigated with

the effects of a single surface protrusion which represents a small fraction of the electrode area, while here, the main focus is on the coupling effects of a collection of protrusions on the breakdown characteristics.

In this work, we aim to study the effects of multiple protrusions with mutual interactions (e.g., electric shielding effect) on microplasma discharge. The breakdown voltages are quantified in the Townsend discharge regime based on the voltage-current curves which are obtained by using a two-dimensional hydrodynamic model. The effects of the protrusion aspect ratio, size, and spacing on the breakdown voltage are studied and the impact of the electric shielding effect on electric potential, ionization rate, and field enhancement are investigated. The breakdown scaling laws are examined in geometrically similar microgaps with the distorted and non-uniform electric field due to the cathode protrusions.

A schematic slice of the microgap in the r–z plane is shown in Fig. 1(a). The microgap consists of two plane-parallel circular electrodes of radius R. A DC voltage U_{dc} is applied to the anode through a ballast resistor $R_b = 100\,k\Omega$ and the cathode is grounded. The concentric protrusions are introduced on the cathode surface with a hemi-elliptical cross-section. A 3D view of the cathode surface is shown in Fig. 1(b), which can be produced with metal micro-droplets using 3D printings.[33] This microstructure incorporates the electric shielding effect among neighboring concentric protrusions, which represents a typical electrode surface morphology and is scalable for larger surfaces to support significant macroscopic current densities that sum to large total current. The shape of protrusions and their configuration are defined by protrusion height a, radial dimension (width) b, and spacing from tip to tip between two neighboring protrusions $X \geq 2b$. The cathode protrusions result in the minimum gap distance $d_{min} = d_{max} - a$ from the anode to the protrusion tip and the maximum gap distance d_{max} from the anode to the cathode substrate. In this model, it is assumed that $d_{max} = 200\,\mu m$ and $R = 500\ \mu m$, unless specified otherwise. With a small aspect ratio of the gap ($d_{max}/R < 0.5$), the gap sidewall is relatively far away from the center and the impact of transverse diffusion on the sidewall of the gap is less important.[34–36]

Argon gas at room temperature (300 K) is chosen as the working gas. The applied voltage ranges from 100 to 200 V, and the gap distance is in the range of 100–200 μm. The maximum electric field is on the order of 10^7 V/m since the space charge is not important and the field enhancement is less than 10 [see Figs. 3(c) and 3(d) below]. The field emission is ignored since the maximum effective electric field is much smaller than the field emission threshold (10^9 V/m).[37,38] The discharge is sustained by the ion-impact secondary electron emission from the cathode. The normal flux of electrons emitted by the cathode is related to the flux of incident ions by an effective secondary emission coefficient γ_{eff}, which is fixed at 0.1.[39,40] At the side wall ($r = R$), the Neumann boundary conditions for species are used and the electric field is evaluated by Gauss's law with surface charge accumulation.[41] Before gas breakdown, the field distribution is close to the Laplace solution since the surface and space charge effects are negligible.[42] The mathematical equations of the discharge model, including species continuity equations, electron energy equation, and Poisson's equation, are solved self-consistently to reach the steady state.[43–45]

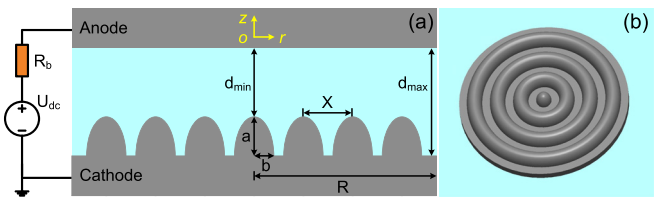

FIG. 1. (a) The schematic of a microgap with concentric protrusions on the cathode surface; (b) a 3D view of the electrode with concentric protrusions.

The breakdown voltage in the microgap is identified using the voltage-current characteristics. By stepping the applied voltage U_{dc} with small intervals in a series of simulations, a typical voltage-current curve, which includes (i) Geiger-Müller regime, (ii) Townsend discharge regime, and (iii) subnormal glow discharge regime, is obtained, as shown in Fig. 2(a). In the Townsend regime, the gap voltage is roughly constant while the discharge current varies across orders of magnitude. The breakdown point is identified when the discharge enters the subnormal glow regime with a negative differential resistance.[46] In Fig. 2(a), for the case $p = 500$ Torr, $a = 50\ \mu m$, $b = 25\ \mu m$, $X = 100\ \mu m$, $d_{max} = 200\ \mu m$, and $R = 500\ \mu m$, the breakdown point is reached when $U_{dc} = 147$ V. Using this method, the breakdown voltage can be quantified with very small uncertainties and alternative criteria avoided. Figure 2(b) shows the cathode current density distribution in the steady state with $U_{dc} = 147$ V. The current density is more pronounced on the protrusion tips and is negligible on the substrate between protrusions. The current density distribution in the radial direction is shown in Fig. 2(c) for different applied voltages around the breakdown threshold. It is observed that the current density on the protrusion tip can be more than one order of magnitude larger than that on the substrate. Meanwhile, the enhanced current density on the protrusion tip decreases as the position moves from the center towards the sidewall. When the applied voltage is increased above the breakdown threshold, the current density distribution is enhanced over orders of the magnitude [see plots for $U_{dc} = 147$ V and 148 V in Fig. 2(c)]; otherwise, it increases gradually as the voltage increases. It should be noted that the breakdown voltage determined here is in the Townsend regime, which is very different from the fast streamer or spark breakdowns, where the space charge effect is important.[10–12,29]

The electric field shielding effect is practically used to block the electric field with conductive barriers, such as a conductive shell, inside which the field strength is ideally zero.[47] This shielding effect is also pronounced on electrode surfaces with multiple protrusions, as shown in Fig. 3. The normalized electric potential $\varphi(r, z)/\varphi_{max}$ and the normalized ionization rate $\alpha(r, z)/\alpha_{max}$ are presented in Figs. 3(a) and 3(b), respectively, with $p = 500$ Torr and $U_{dc} = 147$ V. As shown in Fig. 3(a), the electric potential oscillates along the protrusion surface from the center to the sidewall in a nonlinear fashion. The electric potential is

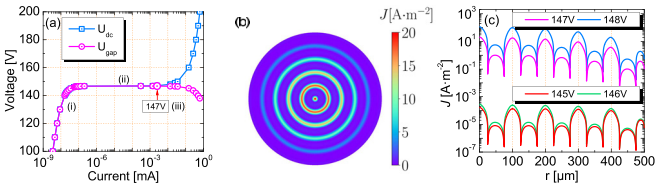

FIG. 2. (a) Voltage-current characteristics with the applied voltage increased from 100 to 200 V; (b) the current density distribution on the cathode with multiple concentric protrusions ($U_{dc} = 147$ V); (c) the radial current density distributions with the applied voltage U_{dc} less ($U_{dc} = 145$ V and 146 V) and larger ($U_{dc} = 147$ V and 148 V) than the breakdown threshold. In this case, $p = 500$ Torr, $a = 50$ μm, $b = 25$ μm, and $X = 100$ μm. The positions of the protrusion tip are at $r = 0$ μm, 100 μm, 200 μm, 300 μm, 400 μm, and 500 μm.

suppressed on the protrusion tip and becomes equipotential between adjacent protrusions due to the electric shielding effect. Away from the cathode region, the effect of surface protrusions on the potential is rapidly smoothed away and the electric potential increases linearly in the axial direction. The ionizations shown in Fig. 3(b) more frequently occur on the protrusion tip rather than on the substrate, which is determined by the geometric electric field enhancement. In Figs. 3(c) and 3(d), it is observed that the normalized electric field $E(z)/E_{av}$ is relatively low at the cathode substrate and reaches its maximum on the protrusion tip, oscillating toward the sidewall roughly as a constant magnitude sinusoid. Note that the average electric field E_{av} is defined as $E_{av} = U_{gap}/d_{max}$. As the protrusion spacing X increases (X = 2*b*, 4*b*, and 8*b*), the shielding effect decreases, and the electric field becomes larger at both the protrusion tip and the cathode substrate. As the aspect ratio a/b becomes smaller, the field enhancement decreases due to flattened protrusions, but other variation characteristics in the radial direction are similar.

Figure 4 shows the effect of the multiple cathode protrusions on the breakdown voltage in the microgap. Figures 4(a) and 4(b) show the impact of the protrusion spacing on the breakdown voltage with different electric shieldings. The

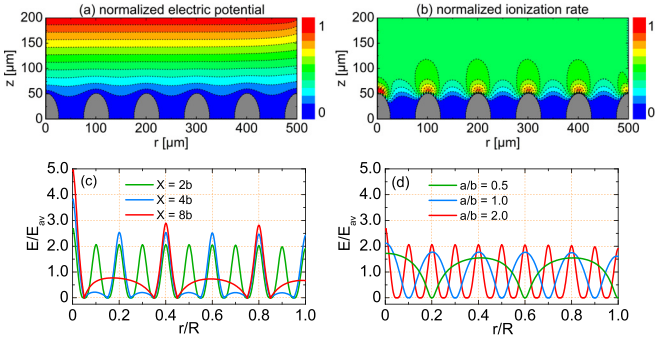

FIG. 3. The spatial distributions of (a) the normalized electric potential $\varphi(r, z)/\varphi_{max}$ for $X = 4b$ and (b) the normalized ionization rate $\alpha(r, z)/\alpha_{max}$ with $p = 500$ Torr and $U_{dc} = 147$ V; the normalized electric field (c) with different spacings between the adjacent protrusions keeping $a = 50$ μm and $b = 50$ μm and (d) with different protrusion aspect ratios keeping $a = 50$ μm and $X = 2b$.

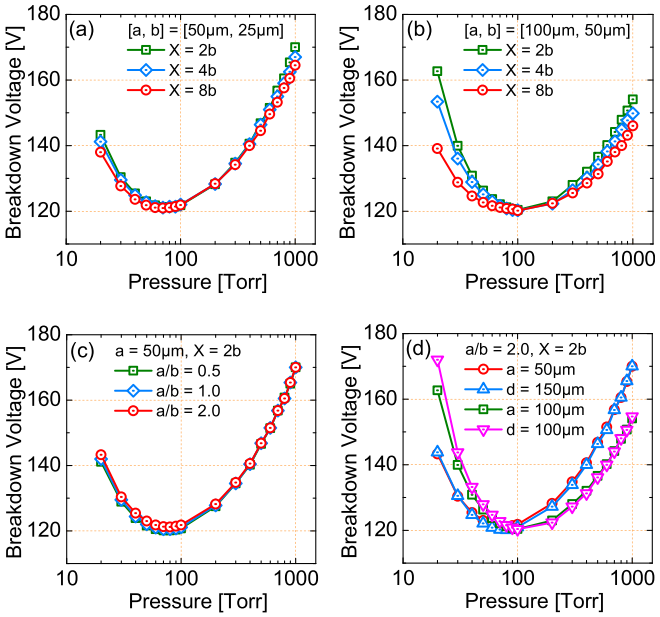

FIG. 4. The calculated breakdown voltage in the microgap ($d_{max} = 200$ μm and $R = 500$ μm) with multiple concentric cathode protrusions. (a) The breakdown voltage curve with different protrusion spacings and $a = 50$ μm and $b = 25$ μm; (b) the breakdown voltage curve with different protrusion spacings and $a = 100$ μm and $b = 50$ μm; (c) the breakdown voltage curve with different protrusion aspect ratios $a/b = 0.5$, 1.0, and 2.0; (d) the breakdown curves with cathode protrusions ($a = 50$ μm and 100 μm, $a/b = 2.0$, and $X = 2b$) compared to the plane-parallel cases ($d = 150$ μm and 100 μm).

protrusion spacing X is set to 2*b*, 4*b*, and 8*b* with $a = 50$ μm and $b = 25$ μm in Fig. 4(a) and $a = 100$ μm and $b = 50$ μm in Fig. 4(b). As the protrusion spacing X increases, the breakdown voltage becomes lower in both low- and high-pressure regimes and remains roughly the same near the lowest point. It should be noted that at low pressures, the breakdown can occur along the longest discharge path in the gap, which was experimentally confirmed previously.[48] At high pressures, the discharge does not expand into the region between the perturbations and the breakdown tends to choose the shortest path. When the protrusion spacing is small, the diffusion losses to the protrusion side walls could also prevent the discharge reaching the cathode substrate and make the long path breakdown ineffective, which is consistent with the increasing shielding effect. The results in Fig. 4(b) are consistent with the electric field enhancement [see Fig. 3(c) above] with larger spacing when the shielding effect becomes weaker and the electric field enhancement becomes larger at both the protrusion tip and the cathode substrate. Therefore, wherever the ionization occurs, on either the protrusion tip or the cathode substrate, it will result in lower breakdown voltage. With a smaller protrusion height, shown in Fig 4(a), the breakdown voltage difference is relatively small since the perturbation of the electric field is smoothed away in a short distance across the gap. With a larger protrusion height, as shown in Fig 4(b), the breakdown voltage difference caused by different shielding effects is more pronounced.

The impact of the different protrusion aspect ratios a/b on the breakdown voltage is shown in Fig. 4(c), when the electric shielding is the most effective ($X = 2b$). The breakdown curves in Fig. 4(c) are overlapping, which indicate that the aspect ratio has little impact on the breakdown voltage. This tells that the breakdown voltage does not change obviously even though the surface protrusions become relatively flat, which inspires us to compare the breakdown curves to the plane-parallel cases with the shortest gap distance ($d = d_{min} = d_{max} - a$). In Fig. 4(d), with $a/b = 2.0$ and $X = 2b$, the cases $a = 50$ μm and $a = 100$ μm correspond to the plane-parallel cases $d = 150$ μm and $d = 100$ μm, respectively. The aspect ratio d/R of the plane-parallel cases is chosen as $d/R = d_{max}/R = 0.4$. In Fig. 4(d), when the protrusion height is smaller ($a = 50$ μm), the breakdown curve with protrusions overlaps the plane-parallel case. When the protrusion height is larger ($a = 100$ μm), the breakdown curve with surface protrusions still overlaps the plane-parallel case ($d = 100$ μm) on the right branch but can be slightly lower on the left branch. Note that the ranges of pd_{min} in Fig. 4(d) with different protrusion heights are not the same and the separation of the breakdown curves also occurs for the case of $a = 50$ μm and the corresponding plane-parallel case ($d = 150$ μm) at lower pressures. Also note that increasing the protrusion height leads to the intersection of breakdown voltage curves, which results in lower (higher) breakdown voltages on the right (left) branch with a larger height. Therefore, the breakdown voltage with multiple cathode protrusions is more sensitive to the protrusion height and can be assessed by the shortest gap distance in plane-parallel geometry when the electric shielding effect is significant.

As is known, scaling laws are essential in understanding breakdown processes at different conditions and predicting discharge properties on different scales.[21–23,34,49–55] The breakdown scaling law based on Townsend theory is usually investigated in cases with plane-parallel gaps when the electric field is uniform.[56,57] Previous studies indicate that Townsend theory is still valid in microdischarges unless the field emission plays a role.[17–19] Even though in the secondary electron emission dominated regime, it is critical to check the validity of the breakdown scaling law while the electric field is distorted and non-uniform due to surface protrusions. In Table I, two pairs of geometrically similar microgaps (cases A1 and A2 and cases B1 and B2) with multiple concentric cathode protrusions are considered. In geometrically similar microgaps, all linear dimensions are proportional via a scaling factor k. Cases A1 and B1 are the original microgaps with $k = 1$ and cases A2 and B2 are the corresponding scaled up microgaps with $k = 2$.

TABLE I. Geometrically similar microgaps with concentric cathode protrusions and k is the scaling factor.

Case no.	d_{max} (μm)	R (μm)	a (μm)	b (μm)	X (μm)
Case A1: ($k = 1$)	200	500	50	25	50
Case A2: ($k = 2$)	400	1000	100	50	100
Case B1: ($k = 1$)	200	500	100	50	100
Case B2: ($k = 2$)	400	1000	200	100	200

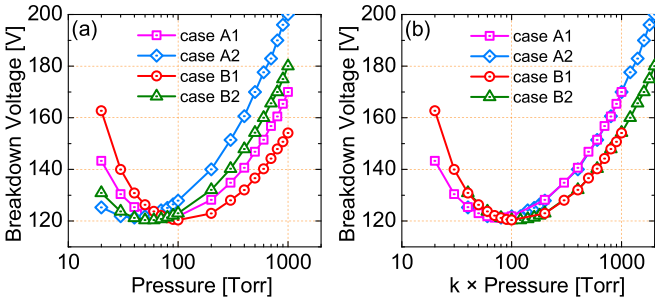

FIG. 5. (a) The breakdown curves as a function of gas pressure for geometrically similar gaps; (b) the breakdown curves as a function of the gas pressure scaled with the corresponding scaling factor k.

Breakdown curves are calculated for the cases A1, A2, B1, and B2 and shown in Fig. 5. It can be seen in Fig. 5(a) that four breakdown curves versus the gas pressure are separated, while in Fig. 5(b), the breakdown curves versus the scaled gas pressure ($k \times$ pressure) are overlapping. Even though the gap distance ranges from d_{min} to d_{max} due to the surface protrusions, the breakdown curve $U_b = f(k \times \text{pressure})$ can be referred to a general Paschen's law. The breakdown scaling law still holds for microgaps with multiple surface protrusions despite the electric field distortion near the cathode, through which the applicability of the scaling laws can be extended.

In summary, breakdown characteristics are investigated in microgaps with multiple concentric cathode protrusions. Based on the voltage-current characteristics, the breakdown voltages are quantified in the Townsend regime when discharges are dominated by secondary electron emission. The results elucidate the effects of competing factors (i.e., electric shielding and field enhancement) on the breakdown characteristics which depend largely on the cathode surface morphology. The breakdown can occur along the longest discharge path at low pressures when the protrusion spacing is larger and the shielding effect is not significant or along the shortest path at high pressures when the electric field is enhanced on the protrusion tips. When the protrusion spacing is small, the shielding effect plays a more important role in the breakdown voltage rather than the protrusion aspect ratio, and the breakdown voltage can be assessed by the shortest gap distance. As the protrusion spacing increases, the electric shielding effect decreases, and the breakdown voltage is lower in both low- and high-pressure regimes. The breakdown scaling law still holds in geometrically similar microgaps with surface protrusions even though the electric field is distorted near the cathode. Although a more accurate description of the discharge may require kinetic treatment of electrons, the proposed method can capture the transition from the Townsend to subnormal glow discharge regime, which can be employed to understand the qualitative trends of the breakdown characteristics in microgaps with protrusion geometries.[58–60] This study provides insight into the design and the operation of microdischarge devices for controlling (triggering or suppressing) the breakdown with engineered surface morphologies using emerging fabrication technologies. The possible

connection of this work to hollow cathode and microcavity discharges could be further explored.[26,61–64] Further work may also include the effect of microstructures on field emission, discharge stability and variability, and plasma source efficiency in microdischarge devices, to further extend the relevant applications.

This work was supported by Air Force Office of Scientific Research (AFOSR) Grant No. FA9550-18-1-0062, and U.S. Department of Energy Plasma Science Center Grant No. DE-SC0001939. Peng Zhang was also supported by AFOSR YIP Award No. FA9550-18-1-0061.

REFERENCES

[1]A. M. Loveless and A. L. Garner, Appl. Phys. Lett. **108**, 234103 (2016).
[2]T. Ito, T. Kanazawa, and S. Hamaguchi, Phys. Rev. Lett. **107**, 065002 (2011).
[3]A. Semnani, A. Venkattraman, A. A. Alexeenko, and D. Peroulis, Appl. Phys. Lett. **102**, 174102 (2013).
[4]K. H. Schoenbach and K. Becker, Eur. Phys. J. D. **70**, 29 (2016).
[5]A. Peschot, N. Bonifaci, O. Lesaint, C. Valadares, and C. Poulain, Appl. Phys. Lett. **105**, 123109 (2014).
[6]J. A. Buendia and A. Venkattraman, Europhys. Lett. **112**, 55002 (2015).
[7]Y. Fu, P. Zhang, J. P. Verboncoeur, A. J. Christlieb, and X. Wang, Phys. Plasmas **25**, 013530 (2018).
[8]A. Pedersen, IEEE Trans. Power Appar. Syst. **94**, 1749 (1975).
[9]S. Berger, IEEE Trans. Power Appar. Syst. **95**, 1073 (1976).
[10]Y. Qiu and I. D. Chalmers, J. Phys. D: Appl. Phys. **26**, 1928 (1993).
[11]A. M. Mahdy, H. I. Anis, and S. A. Ward, IEEE Trans. Dielectr. Electr. Insul. **5**, 612 (1998).
[12]M. Hikita, S. Ohtsuka, N. Yokoyama, S. Okabe, and S. Kaneko, IEEE Trans. Dielectr. Electr. Insul. **15**, 243 (2008).
[13]M. S. M. Saheed, N. M. Mohamed, and Z. A. Burhanudin, Appl. Phys. Lett. **104**, 123105 (2014).
[14]U. Zywietz, A. B. Evlyukhin, C. Reinhardt, and B. N. Chichkov, Nat. Commun. **5**, 3402 (2014).
[15]Y. Kashiwagi, A. Koizumi, Y. Takemura, S. Furuta, M. Yamamoto, M. Saitoh, M. Takahashi, T. Ohno, Y. Fujiwara, K. Murahashi, and K. Ohtsuka, Appl. Phys. Lett. **105**, 223509 (2014).
[16]I. Stefanović, J. Berndt, D. Marić, V. Šamara, M. Radmilović-Radjenović, Z. L. Petrović, E. Kovačević, and J. Winter, Phys. Rev. E **74**, 026406 (2006).
[17]R. Tirumala and D. B. Go, Appl. Phys. Lett. **97**, 151502 (2010).
[18]D. B. Go and D. A. Pohlman, J. Appl. Phys. **107**, 103303 (2010).
[19]D. B. Go and A. Venkattraman, J. Phys. D: Appl. Phys. **47**, 503001 (2014).
[20]D. Levko and L. L. Raja, J. Appl. Phys. **117**, 173303 (2015).
[21]A. Venkattraman and A. A. Alexeenko, Phys. Plasmas **19**, 123515 (2012).
[22]A. M. Loveless and A. L. Garner, Phys. Plasmas **24**, 113522 (2017).
[23]A. M. Loveless and A. L. Garner, IEEE Trans. Plasma Sci. **45**, 574 (2017).
[24]M. Radmilović-Radjenović, Š. Matejčik, M. Klas, and B. Radjenović, J. Phys. D: Appl. Phys. **46**, 015302 (2013).
[25]Y. Fu, J. Krek, P. Zhang, and J. P. Verboncoeur, Plasma Sources Sci. Technol. **27**, 095014 (2018).
[26]S. H. Sung, I. C. Hwang, S. J. Park, and J. G. Eden, Appl. Phys. Lett. **97**, 231502 (2010).
[27]A. Venkattraman, J. Phys. D: Appl. Phys. **47**, 425205 (2014).
[28]T. Shao, W. Yang, C. Zhang, Z. Niu, P. Yan, and E. Schamiloglu, Appl. Phys. Lett. **105**, 071607 (2014).
[29]J. Zhang, Y. Wang, and D. Wang, Phys. Plasmas **25**, 072101 (2018).
[30]A. Semnani, A. Venkattraman, A. A. Alexeenko, and D. Peroulis, Appl. Phys. Lett. **103**, 063102 (2013).
[31]Y. Fu, P. Zhang, and J. P. Verboncoeur, Appl. Phys. Lett. **112**, 254102 (2018).
[32]Y. Fu, P. Zhang, and J. P. Verboncoeur, Appl. Phys. Lett. **113**, 054102 (2018).
[33]M. Zenou, A. Sa'Ar, and Z. Kotler, Sci. Rep. **5**, 17265 (2015).
[34]V. A. Lisovskiy, S. D. Yakovin, and V. D. Yegorenkov, J. Phys. D: Appl. Phys. **33**, 2722 (2000).
[35]V. A. Lisovskiy, N. D. Kharchenko, and V. D. Yegorenkov, J. Phys. D: Appl. Phys. **43**, 425202 (2010).
[36]Y. Fu, H. Luo, X. Zou, and X. Wang, Phys. Plasmas **22**, 023502 (2015).
[37]D. Levko and L. L. Raja, Phys. Plasmas **23**, 073513 (2016).
[38]J. Lin, P. Y. Wong, P. Yang, Y. Y. Lau, W. Tang, and P. Zhang, J. Appl. Phys. **121**, 244301 (2017).
[39]A. V. Phelps and Z. Lj Petrović, Plasma Sources Sci. Technol. **8**, R21 (1999).
[40]A. V. Phelps and B. M. Jelenković, Phys. Rev. A **38**, 2975 (1988).
[41]E. A. Bogdanov, V. I. Demidov, A. A. Kudryavtsev, and A. I. Saifutdinov, Phys. Plasmas **22**, 024501 (2015).
[42]R. Schnyder, A. A. Howling, D. Bommottet, and C. Hollenstein, J. Phys. D: Appl. Phys. **46**, 285205 (2013).
[43]G. J. M. Hagelaar and L. C. Pitchford, Plasma Sources Sci. Technol. **14**, 722 (2005).
[44]T. Farouk, B. Farouk1, D. Staack, A. Gutsol, and A. Fridman, Plasma Sources Sci. Technol. **15**, 676 (2006).
[45]Y. Fu, H. Luo, X. Zou, and X. Wang, Plasma Sources Sci. Technol. **23**, 065035 (2014).
[46]J. T. Gudmundsson and A. Hecimovic, Plasma Sources Sci. Technol. **26**, 123001 (2017).
[47]J. B. Pendry, D. Schurig, and D. R. Smith, Science **312**, 1780 (2006).
[48]D. Marić, N. Škoro, P. D. Maguire, C. M. O. Mahony, G. Malović, and Z. L. Petrović, Plasma Sources Sci. Technol. **21**, 035016 (2012).
[49]Z. L. Petrović, N. Škoro, D. Marić, C. M. O. Mahony, P. D. Maguire, M. Radmilović-Rađenović, and G. Malović, J. Phys. D: Appl. Phys. **41**, 194002 (2008).
[50]N. Škoro, D. Marić, and Z. L. Petrović, IEEE Trans. Plasma Sci. **36**, 994 (2008).
[51]S. K. Nam and J. P. Verboncoeur, Comput. Phys. Commun. **180**, 628 (2009).
[52]Y. Fu, Y. Shuo, X. Zou, H. Luo, and X. Wang, Phys. Plasmas **23**, 093509 (2016).
[53]Y. Fu, Y. Shuo, X. Zou, H. Luo, and X. Wang, Phys. Plasmas **24**, 023508 (2017).
[54]M. U. Lee, J. Lee, J. K. Lee, and G. S. Yun, Plasma Sources Sci. Technol. **26**, 034003 (2017).
[55]M. U. Lee, J. Lee, G. S. Yun, and J. K. Lee, Eur. Phys. J. D **71**, 94 (2017).
[56]J. S. Townsend, *Electricity in Gases* (Clarendon Press, Oxford, 1915).
[57]Y. P. Raizer, *Gas Discharge Physics* (Springer, Berlin, 1991).
[58]R. R. Arslanbekov and V. I. Kolobov, J. Phys. D: Appl. Phys. **36**, 2986 (2003).
[59]E. Arcese, F. Rogier, and J. P. Boeuf, Phys. Plasmas **24**, 113517 (2017).
[60]I. Rafatov and C. Yesil, Phys. Plasmas **25**, 082107 (2018).
[61]K. H. Becker, K. H. Schoenbach, and J. G. Eden, J. Phys. D: Appl. Phys. **39**, R55 (2006).
[62]D. Marić, N. Škoro, G. Malović, Z. L. Petrović, V. Mihailov, and R. Djulgerova, J. Phys.: Conf. Ser. **162**, 012007 (2009).
[63]J. Greenan, C. M. O. Mahony, D. Mariotti, and P. D. Maguire, Plasma Sources Sci. Technol. **20**, 025011 (2011).
[64]J. G. Eden, S. J. Park, J. H. Cho, M. H. Kim, T. J. Houlahan, B. Li, E. S. Kim, T. L. Kim, S. K. Lee, K. S. Kim, J. K. Yoon, S. H. Sung, P. Sun, C. M. Herring, and C. J. Wagner, IEEE Trans. Plasma Sci. **41**, 661 (2013).